Computational Materials Science, in press (2018)

# Computation of virtual X-ray diffraction patterns from discrete dislocation structures

Nicolas Bertin[a,*], Wei Cai[a]

[a] *Department of Mechanical Engineering, Stanford University, Stanford, CA, USA*

**Abstract**

A computational method to generate virtual micro-Laue X-ray diffraction patterns from discrete dislocation representations is presented. In order to capture elastic strain and rotation heterogeneities in space, the method takes a two-step approach, whereby the deformation gradient field is first evaluated at a set of sampling points throughout the volume, after which the diffracting vectors at each sampling point are ray-traced and their intensities are integrated to produce the resulting diffraction patterns. A non-singular formulation for the deformation gradient is developed to avoid numerical artifacts arising when sampling near dislocation cores. As an example, the method is applied to compute virtual diffraction peaks on a large scale strain-hardened microstructure in single crystal copper obtained from a dislocation dynamics simulation.

*Keywords:* X-ray diffraction, Laue pattern, Dislocations

## 1. Introduction

X-ray diffraction (XRD) has long been recognized as a powerful non-destructive technique to characterize the internal structure and the mechanical state of crystalline materials. For example, polychromatic synchrotron X-ray sources allowing for submicron spatial resolution have been widely employed in metals to study the plastic deformation at different stages [1–5]. The success of such techniques owes much to the fact that diffraction patterns, e.g. micro-Laue patterns, are sensitive to dislocations content and arrangements. While the broadening of diffraction peaks is associated with strain gradients, the occurrence of long, sometimes discontinuous diffraction streaks typically results from the presence of geometrically necessary boundaries [6, 7]. Intensity distributions can be further used to estimate dislocation density tensors and their distribution on the different slip systems [8].

*Corresponding author

*Email address:* nbertin@stanford.edu (Nicolas Bertin)

Concurrently to developments in experimental techniques, significant progress have been made in recent years regarding numerical simulation methods, such as Discrete Dislocation Dynamics (DDD), which simulate the evolution of dislocation microstructure in crystals during plastic deformation [9]. For instance, the recent development of efficient numerical integration schemes have allowed DDD simulations to generate increasingly complex microstructures in large representative volume elements [10].

Yet, few direct comparisons have been made between experimental and simulated dislocation structures. Transmission electron microscopy (TEM) was for instance used in [11] to compare dislocation motion in thin film Cu foils with DDD simulations. However, TEM characterization of dislocations is usually not straightforward and suffers from several artifacts. Specifically, thin foils need to be cut from a bulk sample, making the resulting observations strongly dependent on the foil orientation, i.e. the plane of cut. In addition, the creation of free surfaces during the cutting procedure usually alters the dislocation structure, which rearranges locally and no longer retains the characteristics of the bulk. This effect was for instance reported in [11] where the dislocation behavior was found to be mainly governed by surface forces.

Alternatively, XRD analysis appears as a convenient and powerful means of comparison between experimental and simulations results. Of particular interest, XRD operates as a non-destructive technique and does not suffer from the same limitations associated with TEM sample preparation. Specifically, it can be employed to analyze bulk microstructures, possibly *in situ*, and without the introduction of probing artifacts.

Several approaches have been recently developed to generate virtual diffraction patterns from discrete defects modeling. For instance, Hofmann *et al.* established a ray-tracing framework [12] that was later applied to study the diffraction maps resulting from the presence of a single Frank-Read source modeled in DDD [13]. As an other approach, several numerical techniques based on the powder diffraction formalism were proposed and investigated in [14, 15] to enable virtual line profile analysis. However, one common limitation of these approaches stems from the fact that they all rely on the classical theory of elasticity to evaluate the displacement or strain fields of dislocations. As such, their values may become unbounded as one approaches dislocations cores, potentially leading to numerical artifacts. As a result, previous methods have only been applied to the cases of relatively simple structures, and are not suitable for complex discrete structures in their present formulations.

In this paper, we propose a non-singular approach to compute virtual diffraction patterns from discrete dislocation structures in single crystals based on the ray-tracing algorithm presented in [12]. To this end, an analytical formulation for the deformation gradient arising from an arbitrary finite dislocation segment

is derived based on the isotropic Burgers distribution introduced in [16]. The diffraction patterns are then constructed by ray-tracing the diffracted vectors associated with crystallographic reflections and integrating their intensity over a large number of material sampling points. During this process, a regularization procedure is applied to eliminate the conditional convergent behavior associated with periodic image sums. The approach is applied to generate virtual diffraction maps for different dislocation microstructures with increasing complexity. To increase the efficiency of the method, a GPU-accelerated implementation is developed.

The paper is organized as follows. In section 2, the numerical ray-tracing approach to compute the diffraction vectors for each crystallographic plane at a given material point is first reviewed in §2.1, while the non-singular displacement gradient formulation is presented in §2.2. The general algorithm is then summarized in §2.3. In section 3, the validity of the approach is first tested via examination of tilt and twist grain boundary configurations. In §3.2, the method is then employed to produce virtual diffraction patterns for a complex strain-hardened DDD microstructure, where the effects of periodicity, diffraction volume size, and dislocation core radius are examined. The numerical implementation, the performance of the method and its GPU version are discussed in §3.3. A summary is given in section 4.

## 2. Methodology

### *2.1. Virtual diffraction patterns generation*

Virtual Laue diffraction patterns can be generated using the ray-tracing procedure presented in [12], which is briefly summarized in this section. Consider a crystallographic unit cell with primitive underformed crystal coordinate system $(\mathcal{O}, \boldsymbol{a}_1^0, \boldsymbol{a}_2^0, \boldsymbol{a}_3^0)$, and a laboratory Cartesian coordinate system $(\mathcal{O}, \hat{\boldsymbol{e}}_1, \hat{\boldsymbol{e}}_2, \hat{\boldsymbol{e}}_3)$ with the same origin $\mathcal{O}$. Let $\boldsymbol{A}_0$ be the matrix whose column vectors are formed by the real-space lattice vectors $\boldsymbol{a}_1^0$, $\boldsymbol{a}_2^0$, $\boldsymbol{a}_3^0$. As such, $\boldsymbol{A}_0$ maps any position $(u, v, w)^{\mathrm{T}}$ specified in terms of the crystal lattice vectors to the Cartesian coordinate system such that $\boldsymbol{r}_{uvw} = \boldsymbol{A}_0 (u, v, w)^{\mathrm{T}} = u\boldsymbol{a}_1^0 + v\boldsymbol{a}_2^0 + w\boldsymbol{a}_3^0$ (e.g. see [17]). Similarly, if one denotes by $\boldsymbol{B}_0$ the matrix whose columns vectors are formed by the reciprocal space vectors $\boldsymbol{b}_1^0$, $\boldsymbol{b}_2^0$, $\boldsymbol{b}_3^0$, then $\boldsymbol{B}_0$ maps any vector $(h, k, l)^{\mathrm{T}}$ specified in terms of reciprocal space lattice vectors to the Cartesian coordinate system such that $\boldsymbol{q}_{hkl} = \boldsymbol{B}_0 (h, k, l)^{\mathrm{T}} = h\boldsymbol{b}_1^0 + k\boldsymbol{b}_2^0 + l\boldsymbol{b}_3^0$. The relationship between real and reciprocal space vectors can be summarized by $\boldsymbol{B}_0^{\mathrm{T}} = \boldsymbol{A}_0^{-1}$.

Deformation of the crystal changes the transformation matrices $\boldsymbol{A}_0$ and $\boldsymbol{B}_0$ to $\boldsymbol{A}$ and $\boldsymbol{B}$, respectively, which are given by:

$$\boldsymbol{A} = (\boldsymbol{I} + \boldsymbol{G})\boldsymbol{A}_0 \tag{1}$$

$$\boldsymbol{B} = \left[(\boldsymbol{I} + \boldsymbol{G})^{-1}\right]^{\mathrm{T}} \boldsymbol{B}_0 \tag{2}$$

where $\boldsymbol{I}$ denotes the identity matrix, and $\boldsymbol{G}$ is the deformation gradient expressed in the laboratory frame, which contains both the elastic strain $\boldsymbol{\varepsilon}$ and rotation $\boldsymbol{\omega}$ tensors, given by its symmetric and anti-symmetric parts, respectively.

In the deformed crystal, $\boldsymbol{q}_{hkl} = \boldsymbol{B}\,(h,k,l)^{\mathrm{T}}$ is the diffraction vector associated with the crystallographic plane with Miller indices $hkl$, and $d_{hkl} = \|\boldsymbol{q}_{hkl}\|$ and $\hat{\boldsymbol{n}}_{hkl} = \boldsymbol{q}_{hkl}/d_{hkl}$ are the spacing and the unit normal of the $hkl$ planes, respectively. When an incident beam $\hat{\boldsymbol{s}}_0$ is shone at a given location on the deformed crystal, the scattered vector $\hat{\boldsymbol{s}}$ reflected off a given $hkl$ plane is given by

$$\hat{\boldsymbol{s}} = \hat{\boldsymbol{s}}_0 - 2(\hat{\boldsymbol{s}}_0 \cdot \hat{\boldsymbol{n}}_{hkl})\hat{\boldsymbol{n}}_{hkl} \tag{3}$$

From there, the scattered vectors $\{\hat{\boldsymbol{s}}\}$ associated with all diffracting $hkl$ planes can be ray-traced to generate virtual diffraction patterns. Specifically, let us consider the setting illustrated in figure 1(a), where a detector with surface dimensions $(l_x, l_y)$ and axes $(\hat{\boldsymbol{x}}_d, \hat{\boldsymbol{y}}_d)$ is positioned at location $\boldsymbol{D}$. Here $\boldsymbol{D}$ denotes the vector linking the scattering center $S$ to the detector center $O$. If one denotes $\boldsymbol{d}$ the projection of the scattering center $S$ on the detector plane, the position of spot $R$ – produced by reflected beam $\hat{\boldsymbol{s}}$ on the detector surface – can be located with vector $\boldsymbol{P}$ from the detector center $O$ as

$$\boldsymbol{P} = (\boldsymbol{d} - \boldsymbol{D}) + \frac{\|\boldsymbol{d}\|}{(\hat{\boldsymbol{s}} \cdot \hat{\boldsymbol{d}})}\left(\hat{\boldsymbol{s}} - (\hat{\boldsymbol{s}} \cdot \hat{\boldsymbol{d}})\hat{\boldsymbol{d}}\right) \tag{4}$$

where $\hat{\boldsymbol{d}} = \boldsymbol{d}/\|\boldsymbol{d}\|$. To reproduce experimental conditions in which diffraction patterns are typically captured on a CCD sensor, the spot position $R$ is converted to pixel coordinates $(r_i, r_j)$ by binning vector $\boldsymbol{P}$ into the surface grid of the detector

$$(r_i, r_j) = \left(\left\lceil\left(\boldsymbol{P} \cdot \hat{\boldsymbol{x}}_d + \frac{l_x}{2}\right)\frac{N_x}{l_x}\right\rceil, \left\lceil\left(\boldsymbol{P} \cdot \hat{\boldsymbol{y}}_d + \frac{l_y}{2}\right)\frac{N_y}{l_y}\right\rceil\right) \tag{5}$$

where $N_x$ and $N_y$ are the number of pixels of the detector along the $\hat{\boldsymbol{x}}_d$ and $\hat{\boldsymbol{y}}_d$ directions respectively, and $\lceil x \rceil$ denotes the ceiling function.

Using equations (4) and (5), the coordinates of the reflected spot produced by each diffracting $hkl$ plane can be determined at a given material point. However, not all allowed reflections will produce a spot on the detector. First, a reflected beam is not guaranteed to fall within the detector angular range, i.e. no spot will be produced when $(r_i, r_j) \notin [1, N_x] \times [1, N_y]$. Second, an incident beam will be

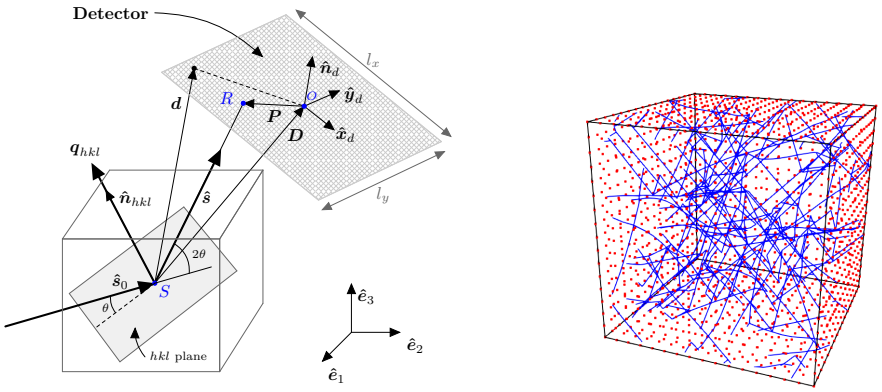


(a) (b)

Figure 1: (a) Schematic of the ray-tracing technique used to compute the virtual diffraction spot $R$ produced on a detector by reflection of an incident beam $\hat{\boldsymbol{s}}_0$ on crystallographic plane with $hkl$ Miller indices at a given position in a crystal. The location of spot $R$ is obtained by computing the intersection between the reflected ray with direction $\hat{\boldsymbol{s}}$ and the detector plane. (b) Example of a dislocation microstructure and sampling points in the simulation volume.

reflected off a given $hkl$ plane only if the scattered beams interfere constructively, i.e. when Bragg's law,

$$n\lambda = 2d_{hkl}\sin\theta \tag{6}$$

is satisfied. In equation (6), $n$ is an integer corresponding to the order of the reflection, $\lambda$ is the wavelength of the incident beam, and $\theta$ is the incidence angle (see figure 1(a)) given by

$$\theta = \arcsin\left(\hat{\boldsymbol{s}}_0 \cdot \hat{\boldsymbol{n}}_{hkl}\right) = \frac{1}{2}\arccos\left(\hat{\boldsymbol{s}}_0 \cdot \hat{\boldsymbol{s}}\right) \tag{7}$$

In the context of a micro-Laue experiment in which a white-beam is typically used, Bragg's law can be enforced by ensuring that the energy $E_{hkl}$ associated with the reflection is contained within the energy spectrum $\mathcal{E}_{\text{beam}}$ of the incident beam, i.e.

$$E_{hkl} = \frac{hc}{\lambda} = \frac{hc}{2d_{hkl}\sin\theta} \in \mathcal{E}_{\text{beam}} \tag{8}$$

where $h$ and $c$ are the Planck constant and the speed of light in vacuum, respectively. When condition (8) is not satisfied, the intensity of the reflection is assumed to be too weak for the detector to capture it. If condition (8) is satisfied, the coordinates $(r_i, r_j)$ of the reflected spot $R$ are computed using expression (5), and the detector intensity entry $I(r_i, r_j)$ of the corresponding pixel is incremented, i.e.

$$I(r_i, r_j) = \sum_{hkl} I_{hkl} \cdot f(E_{hkl}) \tag{9}$$

where the sum is carried over all $hkl$ reflections satisfying relation (8) that produce a spot at pixel $(r_i, r_j)$, $f(E_{hkl})$ is the power spectrum distribution function associated with the incoming beam, and $I_{hkl}$ is an intensity function associated with the $hkl$ reflection. In the rest of this work, the intensity is taken as $I_{hkl} = |F_{hkl}|^2$, where $F_{hkl}$ denotes the structure factor.

The primary objective of this work is to generate virtual diffraction from microstructures obtained from DDD simulations, for which an example is shown in figure 1(b). In this context, the deformation gradient field $\boldsymbol{G}$ is expected to be highly non-uniform throughout the material volume $V$. This effect is amplified by the discrete nature of dislocation lines representation in DDD simulations, and by the fact that such lines typically form complex arrangements. In order to generate XRD patterns that captures the heterogeneous nature of the structure, a volume integral of the intensities of the diffracted rays must be performed. Numerically, this can be achieved by discretizing the simulation volume $V$ into a regular grid of $N_s$ sampling points $\{\boldsymbol{x}_s\}_{s=1,\dots,N_s}$ (see figure 1(b)) and ray-tracing all $hkl$ reflections given the local deformation gradient $\boldsymbol{G}(\boldsymbol{x}_s)$ at each grid point. During this process, the scattering center $S$ associated with each voxel $s$ is located at position $\boldsymbol{x}_s$, such that vector $\boldsymbol{D}$ in expression (4) is different for each sampling point. From there, the global diffraction pattern can be constructed by integrating the pixel intensity (9) over all sampling points.

When considering microstructures generated from DDD simulations, the most challenging part of the above procedure lies in the computation of the deformation gradient $\boldsymbol{G}(\boldsymbol{x}_s)$ that must account for the contribution from every dislocation segments present in the volume (and of their periodic images when periodic boundary conditions are applied), and be evaluated at every sampling point $\boldsymbol{x}_s$. The approach to perform this calculation is presented in details in the next section.

### *2.2. Non-singular deformation gradient*

In this section, the approach devised to compute the deformation gradient throughout a DDD simulation volume is presented. The displacement field induced by a dislocation loop in an infinite elastically isotropic medium is given in [18] as

$$u_m(\boldsymbol{x}) = -\frac{1}{8\pi}\int_S b_m \frac{\partial}{\partial x'_j}\nabla'^2 R\, dS_j - \frac{1}{8\pi}\oint_C b_i \epsilon_{mik}\nabla'^2 R\, dx'_k - \frac{1}{8\pi(1-\nu)}\oint_C b_i \epsilon_{ijk}\frac{\partial^2 R}{\partial x'_m \partial x'_j} dx'_k \tag{10}$$

where $\lambda$ and $\mu$ are the Lamé constants of the medium, $\epsilon_{ijk}$ is the permutation tensor, $\boldsymbol{b}$ is the Burgers vectors of the dislocation loop whose contour $C$ delineates the boundary over the cut surface $S$, and $R = \|\boldsymbol{x'} - \boldsymbol{x}\|$ is the norm of the distance vector linking the field point $\boldsymbol{x}$ and the coordinate $\boldsymbol{x'}$ that spans the dislocation line.

It can be shown that the deformation gradient $G_{ml} = u_{m,l}$ produced by the dislocation loop can be written as (see Appendix A):

$$u_{m,l}(\boldsymbol{x}) = -\frac{1}{8\pi}\oint_C b_m \epsilon_{jlk} R_{,ppj} dx'_k - \frac{1}{8\pi}\oint_C b_i \epsilon_{mik} R_{,ppl}\, dx'_k - \frac{1}{8\pi(1-\nu)}\oint_C b_i \epsilon_{ijk} R_{,mjl}\, dx'_k \tag{11}$$

where $R_{,ijk} = \partial^3 R/\partial x_i \partial x_j \partial x_k$. Note that from equations (10) to (11) we have switched the derivatives from $x'_i$ to $x_i$.

The expression of the displacement gradient given in equation (11) contains a singularity when evaluated on the dislocation line, i.e. when $\boldsymbol{x} = \boldsymbol{x'}$. This is because the Green's function and its derivatives become unbounded as $R \to 0$ in the classical theory of elasticity, owing to the Dirac delta function description of the dislocation core. In the context of the generation of virtual diffraction patterns, the use of a singular formulation is expected to cause numerical issues; as the displacement gradient needs to be evaluated at a large number of sampling points, the likelihood of taking an evaluation of expression (11) in the vicinity of a dislocation core is very high, and any such evaluation would likely corrupt the numerical results.

To address this issue, we propose a non-singular expression for the displacement gradient based on a non-singular dislocation formulation [16]. In this approach, the singularity is removed by spreading the Burgers vector around the dislocation core. Following the isotropic Burgers distribution proposed in [16], the singularity in expression (11) can be eliminated by employing a modified radius vector $R_a$ defined as:

$$R_a = \sqrt{R^2 + a^2} = \sqrt{R_i R_i + a^2} = \sqrt{(x'_i - x_i)(x'_i - x_i) + a^2} \tag{12}$$

where parameter $a$ denotes the dislocation core width, and $R = \|\boldsymbol{x'} - \boldsymbol{x}\|$ is the original radius vector. With this, and considering that dislocation loop $C$

with Burgers vector $\boldsymbol{b}$ is approximated by a polygonal loop composed of straight dislocation segments, the non-singular expression of the displacement gradient for each segment $\alpha\beta$ is obtained from equation (11) as:

$$u^{\alpha\beta}_{m,l}(\boldsymbol{x}) = -\frac{1}{8\pi}\int_{\boldsymbol{x}_\alpha}^{\boldsymbol{x}_\beta} b_m \epsilon_{jlk} R_{a,ppj}\, dx'_k - \frac{1}{8\pi}\int_{\boldsymbol{x}_\alpha}^{\boldsymbol{x}_\beta} b_i \epsilon_{mik} R_{a,ppl}\, dx'_k - \frac{1}{8\pi(1-\nu)}\int_{\boldsymbol{x}_\alpha}^{\boldsymbol{x}_\beta} b_i \epsilon_{ijk} R_{a,mjl} dx'_k \tag{13}$$

where $\boldsymbol{x}_\alpha$ and $\boldsymbol{x}_\beta$ denote the positions of the segment end points. Since expression (13) does not contain any singularity, a coordinate-independent analytical formulation of the displacement gradient can be obtained by employing an appropriate parametrization. Details on the analytical results are provided in Appendix B. Our formulation was validated by numerically verifying that the displacement gradient expression, when multiplied by the elastic constants, produces the same stress field as that provided in [16].

In addition to providing a consistent approach to the non-singular stress calculation employed in many DDD codes, the use of the non-singular displacement gradient offers a way to (1) control the effect of the dislocation core on the virtual diffraction patterns via the core radius parameter $a$, and (2) examine the convergence behavior with respect to the sampling point density.

Finally, by virtue of the superposition principle, the total elastic deformation gradient at a material point $\boldsymbol{x}$ in the volume is obtained by addition of the contribution associated with each dislocation segment $\alpha\beta$ as

$$G^{\mathrm{tot}}_{ml}(\boldsymbol{x}) = u^{\mathrm{tot}}_{m,l}(\boldsymbol{x}) = \sum_{\alpha\beta} u^{\alpha\beta}_{m,l}(\boldsymbol{x}) \tag{14}$$

When periodic boundary conditions (PBC) are prescribed to the simulation volume $V$, the contribution of image segments is included in expression (14) by periodically replicating the dislocation content of the primary volume. Importantly, it can be shown that, when PBC are used, the sum in (14) over the dislocation image segments is not absolutely convergent, owing to the $1/R^2$ decay of the deformation gradient for elementary segments [19]. A procedure to regularize such a behavior is provided in Appendix C.

### *2.3. General algorithm*

The overall procedure to compute a virtual diffraction pattern from a given microstructure can be summarized as follows:

- Select a diffraction setting by specifying the direction $\hat{\boldsymbol{s}}_0$ and energy range $\mathcal{E}_{\mathrm{beam}}$ of the incident beam, the position and orientation of the detector, and the number $N_s$ of sampling points $\{\boldsymbol{x}_s\}$ to be used

- For each sampling point $\boldsymbol{x}_s$
  - Compute the deformation gradient $\boldsymbol{G}^{\mathrm{tot}}(\boldsymbol{x}_s)$ induced by the presence of all dislocation segments using expressions (13) and (14)
- Compute the average deformation gradient $\boldsymbol{G}^0 = \langle \boldsymbol{G}^{\mathrm{tot}}(\boldsymbol{x}_s) \rangle$ over all sampling points and evaluate the error tensor $D_{ijk}$ arising from the conditional convergence (see Appendix C).
- For each sampling point $\boldsymbol{x}_s$
  - Compute the regularized deformation gradient $\boldsymbol{G}^{\mathrm{PBC}}(\boldsymbol{x}_s)$ (see expression (C.5))
  - For each allowed reflection $hkl$
    - Compute the reflected beam $\hat{\boldsymbol{s}}$ using $\boldsymbol{G}^{\mathrm{PBC}}(\boldsymbol{x}_s)$ and equation (3)
    - Determine if Bragg's condition is satisfied using relation (8)
    - Determine the pixel coordinate $(r_i, r_j)$ (equation (5)) of the reflected spot and increment the corresponding intensity entry $I^s(r_i, r_j)$ (equation (9)) if the spot falls onto the detector surface
- Integrate the intensity arrays $I^s$ calculated at each sampling point to generate the overall virtual diffraction pattern

For the sake of efficiency, a list of all $hkl$ crystallographic planes is pre-generated up to a given order at the beginning of the calculation. In doing so, all forbidden reflections can be directly eliminated.

## 3. Results and discussion

### *3.1. Bi-crystals with low-angle grain boundaries*

As a benchmark, the displacement gradient and diffraction pattern obtained for bi-crystals with low-angle tilt and twist grain boundaries is investigated. To model the tilt grain boundaries (GB), two equidistant periodic arrays of 10 infinite edge dislocations with regular spacing $d = 100b$ are considered, as illustrated in figure 2(a). The edge dislocation lines are aligned along the [001] direction and regularly stacked in the [010] direction, creating GBs on the $yz$-plane. The two arrays are composed of dislocations of opposite signs, i.e. with Burgers vectors pointing in the [100] and $[\bar{1}00]$ directions, respectively.

Similarly, the twist GBs are modeled by considering two sets of perpendicular screw dislocations with regular spacing $d = 100b$, as depicted in figure 2(d). Each set is composed of two perpendicular arrays of 10 screw dislocations: one array with [010] line direction and [001] stacking direction, and the other with [001] line

direction and [010] stacking direction. Both sets have opposite Burgers vector signs. In both cases, periodicity is prescribed in all three spatial directions to model infinite GBs.

For both these GB representations, the misorientation angle $\theta^{\mathrm{mis}}$ between the two crystal regions is simply expressed as [20]:

$$\theta^{\mathrm{mis}} = \frac{b}{d} = 0.01 \text{ rad} \tag{15}$$

Alternatively, the misorientation angle $\theta^{G}$ can be numerically evaluated from the deformation gradient through the elastic rotation

$$\boldsymbol{\omega} = \frac{1}{2}\boldsymbol{\nabla} \times \boldsymbol{u} \qquad \text{or} \qquad \omega_i = \frac{1}{2}\epsilon_{ijk}u_{k,j} = \frac{1}{2}\epsilon_{ijk}G_{kj} \tag{16}$$

In the case of the tilt GBs configuration, $\theta^{G}$ corresponds to the jump in the component of $\boldsymbol{\omega}$ along the dislocation line direction when crossing one of the GBs, i.e. $\theta^{G}_{\mathrm{tilt}} = [\omega_3]$. In contrast, the misorientation angle associated with the twist configuration is obtained as the jump in the elastic rotation along the GBs normal directions, i.e. $\theta^{\mathrm{G}}_{\mathrm{twist}} = [\omega_1]$.

The elastic rotation angle $\omega_3$ calculated from the non-singular deformation gradient for the tilt GBs setting is reported in figures 2(b)-(c). It is observed that the converged value of the misorientation angle $\theta^{\mathrm{G}}_{\mathrm{tilt}} = [\omega_3] \approx 0.01$ rad obtained across the GBs matches the theoretical value $\theta^{\mathrm{mis}}$, while the crystal rotation $\omega_3$ appears to be uniform and of opposite sign on both sides of the boundaries. Similar results are obtained in the case of the twist GBs configuration. As reported in figure 2(e)-(f), the presence of the two opposite sets of criss-crossed screw dislocations generates a uniform elastic rotation within each grain, with a misorientation of magnitude $\theta^{\mathrm{G}}_{\mathrm{twist}} = [\omega_1] \approx 0.01$ rad when crossing each GB. For both settings, it is also observed that the values of the deformation gradient field rapidly converge as the number of periodic images in each direction $N_{\mathrm{img}}$ increases, as a result of the regularization procedure detailed in Appendix C.

An example of a virtual Laue diffraction pattern computed using the method presented in section 2 is reported in figure 3 for a FCC Cu crystal with lattice parameter $a_{\mathrm{lat}} = 3.606$ nm. The pattern is that obtained on a detector normal to the incoming white beam of energy range $\mathcal{E}_{\mathrm{beam}} = [5, 25]$ keV shone along the [100] crystallographic direction, and the parameters used for the calculation are listed in table 1. For the sake of comparison, details of the $(13\bar{1})$ and $(24\bar{2})$ reflections obtained for a perfect crystal (i.e. with no dislocation) and for the tilt GBs configuration are reported in figure 3(b) and (c), respectively.

When no defect are present, each reflection produces a single spot on the detector, with intensity proportional to the square magnitude of their corresponding structure factor. In contrast, each reflection produces two close but well separated spots on the detector when the two tilt GBs are present, as clearly observed

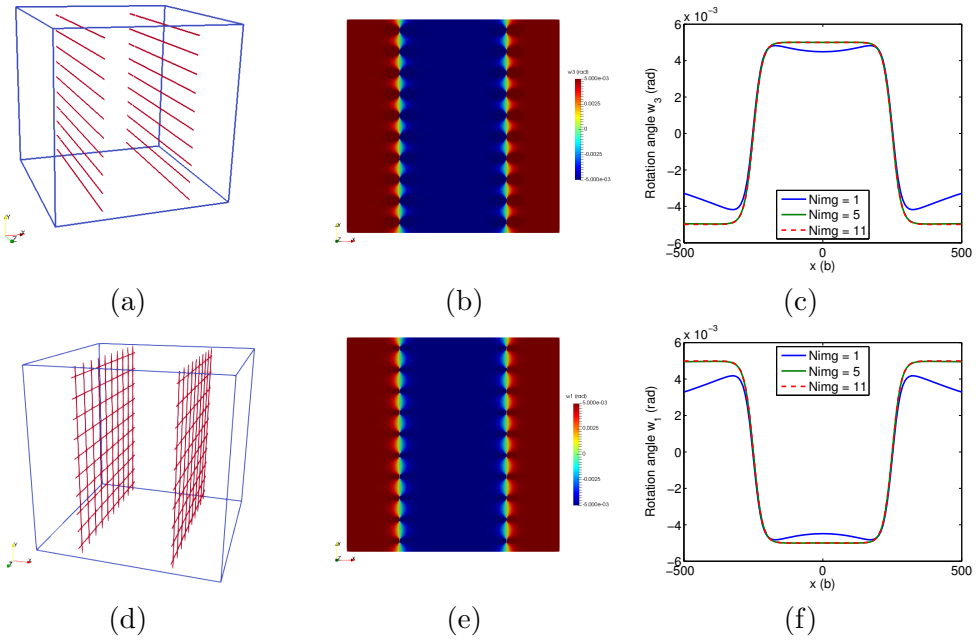


Figure 2: (a-c) Low-angle tilt grain boundaries. (a) Edge dislocations arrays setting to model the tilt GBs. Periodicity is prescribed in all three directions. (b) Rotation angle $\omega_3$ in a plane perpendicular to the dislocations line direction calculated using the non-singular displacement gradient. (c) Rotation angle $\omega_3$ along a line orthogonal to the GB planes as a function of the number of periodic replicas $N_{\text{img}}$ in each direction. (d-f) Low-angle twist grain boundaries. (d) Criss-crossed screw dislocations arrays to model the twist GBs. (e) Rotation angle $\omega_1$ in a plane perpendicular to the twist GBs. (f) Rotation angle $\omega_1$ along a line orthogonal to the GB planes as a function of $N_{\text{img}}$.

for the $(13\bar{1})$ and $(24\bar{2})$ reflections reported in figures 3(b-c), for instance. As expected, this splitting directly results from the fact that each crystallographic plane, whose orientation slightly differs on both sides of the GBs, produces two distinct diffracted rays.

### *3.2. Large scale strain-hardened microstructure*

We now consider the case of a complex dislocation microstructure obtained from a large strain-hardening DDD simulation, such as the one depicted in figure 4(a). Such a structure has been obtained from an initial $(15\mu\text{m})^3$ FCC copper periodic configuration with dislocation density $\rho_0 = 0.7\times10^{12}$ m$^{-2}$. The structure was then loaded up to $\gamma = 1.2\%$ shear strain under a constant strain rate of $\dot{\varepsilon} = 10^3$ s$^{-1}$ applied along the highly symmetrical [001] orientation, using the recently developed subcycling integrator [10]. At $\gamma = 1.2\%$, the structure has a dislocation density of $\rho = 2.1 \times 10^{12}$ m$^{-2}$ and contains slightly more than 15000

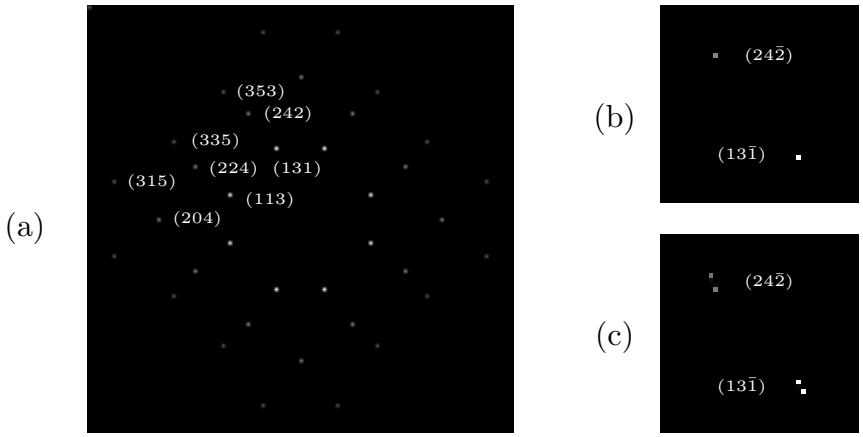


Figure 3: (a) Laue pattern obtained on a detector normal to the the incident beam $\boldsymbol{s}_0$ shone along the [100] crystallographic direction. (b-c) Details for the (13$\bar{1}$) and (24$\bar{2}$) reflections for the (b) perfect crystal and (c) in the presence of tilt GBs. As expected, a splitting of the diffraction vectors is observed for the bi-crystal with tilt GBs in which a uniform elastic rotation is associated with each domain.

dislocation segments.

Detailed intensity maps for the (113) and (204) diffraction peaks computed using an incoming X-ray beam of energy $\mathcal{E}_{\text{beam}} = [5, 25]$ keV shone along the [100] crystallographic direction are shown in figures 4(b) and (c). Each map is obtained on a detector of size $l_x \times l_y = 0.1 \times 0.1$ mm$^2$ and resolution $N_x \times N_y = 128 \times 128$ pixels, and whose center coincides with the position of the diffraction spot that would be produced by a defect-free crystal. The detectors are positioned at a distance $d = 70$ mm from the sample (scattering center) and $N_s = 128^3$ sampling points are used to evaluate the deformation gradient. A number of $N_{\text{img}} = 3$ periodic images in each spatial direction is used for the calculation and the regularization method detailed in Appendix C is employed to correct for the conditional convergent behavior.

It is observed that both diffraction peaks are slightly spread around the detectors center. In comparison, the pattern obtained for a perfect crystal would consist of a very sharp peak at the center of the detector. This phenomenon, referred to as peak broadening, is consistent with experimental observations. Comparing figures 4(b) and (c), it also appears that the diffraction peaks broaden differently for the different reflections. Thus, while the (113) peak shows a rather elongated distribution, the (204) reflection exhibits a slightly more rounded shape for this configuration.

We stress here that the peak broadening effect directly results from the heterogeneous distribution of the deformation gradient throughout the sample. Such

| Parameter designation | Value |
|---|---|
| Shear modulus | $\mu = 54.6$ MPa |
| Poisson ratio | $\nu = 0.324$ |
| Burgers vector | $b = 2.55 \times 10^{-10}$ m |
| Core radius | $a = 6b$ |
| Detector-sample distance | 70 mm |
| Detector size | $200 \times 200$ mm$^2$ |
| Detector resolution | $128 \times 128$ pixels |
| Maximum reflection order | $n = 6$ |

Table 1: Numerical parameters used to generate virtual diffraction patterns

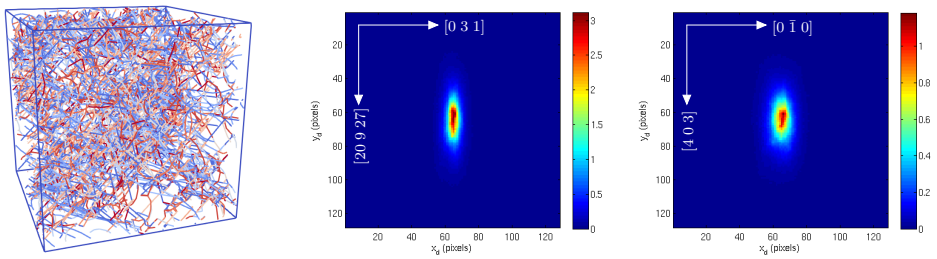


(a) (b) (113) reflection (c) (204) reflection

Figure 4: (a) Dislocation configuration obtained from a DDD simulation loaded with strain rate $\dot{\varepsilon} = 10^3$ s$^{-1}$ at $\gamma = 1.2\%$ shear strain, with dislocation density $\rho = 2.1 \times 10^{12}$m$^{-2}$ in a $(15\mu$m$)^3$ periodic simulation volume. Detailed diffraction peaks obtained for the (b) (113) and (c) (204) crystallographic reflections.

a non-uniform field – produced by the complex arrangements of the dislocation lines – is captured by the sampling approach. To assess the effect of the number of sampling points $N_s$ on the computed patterns, the (204) peak intensity along a row of pixels in the $x_d$ direction passing through the center of the detector is reported in figure 5(a) for uniform sampling grids ranging from $N_s = 16^3$ to $N_s = 256^3$ voxels. While it appears that the computed pattern is very noisy for low resolution sampling grids (e.g. $N_s = 16^3$), the virtual peak profile rapidly converges as the number of sampling points is increased, as attested by the convergence plot shown in the inset. In this last plot, the average deviation of the intensity from a reference map computed for a $N_s = 256^3$ sampling grid is reported as a function of the sampling resolution $N_s$. From this result, we estimate that a resolution of $N_s = 128^3$ sampling points offers a good compromise between accuracy and computation cost for comparable dislocation structures (see section 3.3), although in practice, the use of a lower resolution (e.g. $N_s = 64^3$) is not expected to significantly affect the qualitative insights provided by the virtual

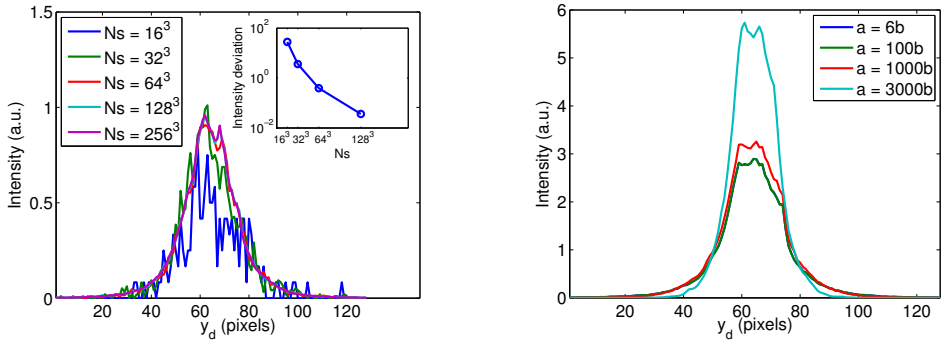


(a) (b)

Figure 5: (a) (204) peak intensity along a row of pixels passing through the center of the detector as a function of the number of sampling points used. Convergence of the peak intensity as a function of the number of sampling points $N_s$ is shown in the inset. The deviation is calculated from a reference peak intensity map computed using $N_s = 256^3$ sampling points. (b) Effect the core radius on the (204) virtual diffraction peak.

XRD patterns.

A critical feature of the method presented in section 2 lies in its non-singular formulation, which ensures that the deformation gradient field can be consistently evaluated at any arbitrary location without returning singular values. Concurrently, the dislocation core radius $a$, introduced to define the amount of spreading of the Burgers vector, becomes a numerical parameter whose effect on the virtual XRD maps should be assessed. For that purpose, the intensity profile of the (204) diffraction peaks obtained for the $(15\mu m)^3$ configuration using $N_s = 128^3$ sampling points has been computed using several values for the core radius. As observed in figure 5(b), it appears that increasing the core width from $a = 6b$ (core value typically used in DD simulations) to $a = 100b$ has an imperceptible effect on the virtual intensity maps. This result is important in that it demonstrates the robustness of the approach with respect to the core radius parameter, i.e. small differences in the choice of the core width do not produce vastly different intensity maps. This effect is explained by the fact that the volume fraction occupied by dislocations cores is typically very small. However, note that when further increasing the core radius to very large values, e.g. $a = 1000b$ and $a = 3000b$, the diffraction peaks become sharper. This effect is explained as follows: as the core radius increases, the Burgers vector distribution is more spread out and the deformation gradient field becomes smoother and weaker, thereby leading to less dispersion in the diffracted vectors.

Finally, note that the results presented so far have been obtained by evaluating the deformation gradient throughout the entire $(15\mu m)^3$ primary cell. In practice however, one could only consider a smaller sub-volume for the calculation of the

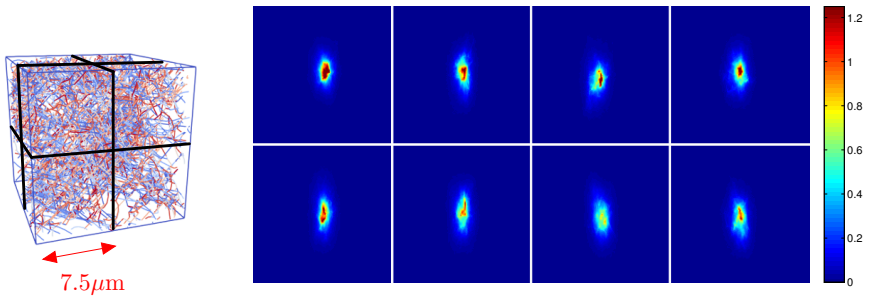


Figure 6: (204) diffraction peak patterns obtained when for each subcell when the $(15\mu m)^3$ primary volume is subdivided into 8 subcells of volume $(7.5\mu m)^3$. The intensity maps obtained for each subcell show noticeable variations, highlighting the spatial heterogeneity of the microstructure.

virtual patterns. In principle, this approach provides a way to establish direct comparisons with diffraction experiments in which the X-ray beam is typically focused on a small volume. Numerically, this can be achieved by prescribing the sampling grid to span only a specific region of the primary cell. (Note that in doing so, the periodicity of the dislocation structure should remain defined over the entire primary supercell).

As an example, the initial $(15\mu m)^3$ simulation cell presented in figure 4(a) is divided into 8 subcells of volume $(7.5\mu m)^3$. The (204) peak diffraction is then calculated independently for each subcell using $N_s = 128^3$ sampling points. Results are presented in figure 6. Interestingly, each subcell produces a slightly different pattern, and in general, the subcell patterns are less symmetrical than patterns obtained from the whole primary volume. These results provide strong evidence for the heterogeneous distribution of the deformation gradient field, i.e. indicating a complex underlying spatial dislocation arrangement. When all subcell patterns are combined together, we have verified that the overall intensity map computed for the whole volume is recovered, thereby demonstrating the consistency of the approach.

### *3.3. Numerical implementation and performance*

As outlined in section 2.3, the computation of diffraction patterns mainly consists in two steps. First, the deformation gradient is evaluated at every sampling points and stored in memory, or in a file. Second, the XRD pattern is generated using the ray-tracing procedure described in section 2.

The first step of the calculation is by far the most expensive in terms of computation time. Overall, it requires $\mathcal{O}(N_{\text{img}}^3 N_{\text{seg}} N_s)$ operations, which are further

associated with a relatively large pre-factor due to the non-trivial expression of the deformation gradient. As a result, it typically accounts for up to 99% of the total computation time. In order to regularize the conditional convergent behavior, the deformation gradient field must be calculated beforehand and stored entirely in memory, requiring $\mathcal{O}(N_s)$ space, or outputted in a file. With this approach, the ray-tracing procedure can be treated as a post-processing step, allowing to efficiently generate several patterns corresponding to various detector features (e.g. location, distance, ...) from a single deformation gradient calculation (the appropriate detector settings to capture a specific peak are not necessarily known *a priori*).

Since the calculation of the deformation gradient at each sampling point is independent from any other sampling point, this step can be parallelized in a straightforward manner by distributing the sampling points across different CPUs. In this work, we also implemented a GPU-accelerated version of the deformation gradient calculation to further increase the efficiency of the method. Similar to the parallel CPU implementation, an efficient GPU implementation is obtained by assigning to each thread the calculation of the deformation gradient at a given sampling point.

In contrast to the deformation gradient calculation, the ray-tracing procedure requires $\mathcal{O}(N_{\text{hkl}}N_s)$ operations, where $N_{\text{hkl}}$ denotes the number of allowed reflections being considered. For instance, when considering reflections up to order $n = 6$ in FCC crystals, the total number of allowed reflections amounts to $N_{\text{hkl}} = 279$.

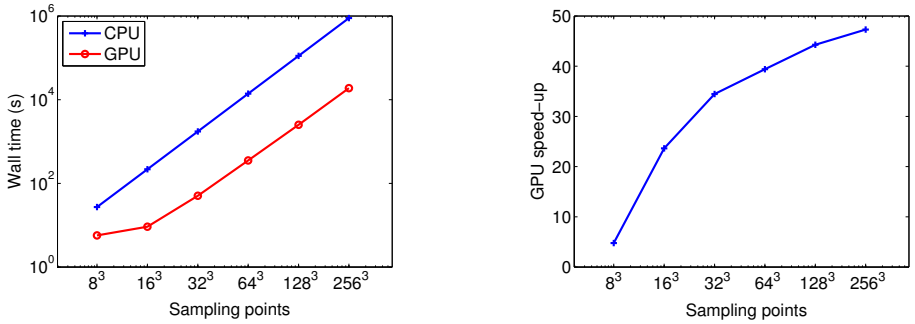


(a) (b)

Figure 7: (a) Wall time (s) required to generate a diffraction pattern for a microstructure with $N_{\text{seg}} \approx 15000$ dislocation segments and considering $N_{\text{img}} = 3$ periodic replica in each direction as function of the number of sampling points $N_s$, for the CPU and the GPU implementations. (b) Speed-up associated with the GPU implementation as a function of the sampling resolution $N_s$. Note that most the computation time is associated with the calculation of the deformation gradient field.

An example of the wall clock time associated with the present approach is shown in figure 7(a). In this figure, the total time required to compute an arbitrary diffraction pattern for a configuration containing approximately $N_{\text{seg}} = 15000$ segments replicated $N_{\text{img}} = 3$ times in each direction is reported as a function of the sampling resolution $N_s$, for the CPU and the GPU implementations. For instance, for a sampling resolution of $N_s = 128^3$ voxels, a virtual XRD map can be generated in approximately 31 hours using a single CPU. In contrast, the GPU-accelerated version (using a Nvidia Titan X device) requires only 40 minutes to perform the same task, thereby providing a speed-up factor of nearly 45, as shown in figure 7(b).

## 4. Conclusion

We presented a method to compute virtual X-ray diffraction patterns from discrete dislocation configurations. By introducing a non-singular formulation for the displacement gradient, the spatial heterogeneities in the elastic fields arising from the dislocation structure are accurately captured by sampling the volume at a large number of points, while ensuring that no numerical artifacts pollute the calculation when sampling close to dislocation cores. A correction procedure is then developed to regularize the conditional convergence arising when evaluating the displacement gradient field under periodic boundary conditions. From there, virtual diffraction patterns are generated by constructing intensity maps using the ray-tracing method. Furthermore, we developed a GPU-accelerated version of the method to increase its computational efficiency and allow for the use of fine sampling resolutions while keeping the computational time low. This approach offers a fast and convenient way to perform direct comparisons between XRD patterns obtained from DDD and experiments.

## Acknowledgement

This work was supported by the U.S. Department of Energy, Office of Basic Energy Sciences, Division of Materials Sciences and Engineering under Award No. DE-SC0010412.

## Appendix A. Derivation of the displacement gradient

The displacement field induced by a dislocation loop in an infinite elastically isotropic medium is given in [18] as

$$u_m(\boldsymbol{x}) = -\frac{1}{8\pi}\int_S b_m \frac{\partial}{\partial x'_j}\nabla'^2 R\, dS_j - \frac{1}{8\pi}\oint_C b_i \epsilon_{mik}\nabla'^2 R\, dx'_k - \frac{1}{8\pi(1-\nu)}\oint_C b_i \epsilon_{ijk}\frac{\partial^2 R}{\partial x'_m \partial x'_j} dx'_k \tag{A.1}$$

where $\lambda$ and $\mu$ are the Lamé constants of the medium, $\epsilon_{ijk}$ is the permutation tensor, $\boldsymbol{b}$ is the Burgers vectors of the dislocation loop whose contour $C$ delineates the boundary over the cut surface $S$, and $R = \|\boldsymbol{x'} - \boldsymbol{x}\|$ is the norm of the radius vector linking the field point $\boldsymbol{x}$ and the coordinate $\boldsymbol{x'}$ that spans the dislocation line. Noting that

$$\nabla'^2 R = \frac{\partial^2 R}{\partial x'_p \partial x'_p} \tag{A.2}$$

equation (A.1) can be written as

$$u_m(\boldsymbol{x}) = -\frac{b_m}{4\pi}\Omega - \frac{1}{8\pi}\oint_C b_i \epsilon_{mik}\frac{\partial^2 R}{\partial x'_p \partial x'_p}\, dx'_k - \frac{1}{8\pi(1-\nu)}\oint_C b_i \epsilon_{ijk}\frac{\partial^2 R}{\partial x'_m \partial x'_j}\, dx'_k \tag{A.3}$$

where $\Omega$ is the solid angle of the loop seen at point $\boldsymbol{x}$ and given by

$$\Omega = \frac{1}{2}\int_S \frac{\partial^3 R}{\partial x'_p \partial x'_p \partial x'_j}\, dS_j \tag{A.4}$$

The deformation gradient $G_{ml} = u_{m,l}$ is directly obtained by differentiating expression (A.3) with respect to the field coordinate:

$$u_{m,l}(\boldsymbol{x}) = -\frac{b_m}{4\pi}\frac{\partial\Omega}{\partial x_l} - \frac{1}{8\pi}\oint_C b_i \epsilon_{mik}\frac{\partial^3 R}{\partial x_l \partial x'_p \partial x'_p}\, dx'_k - \frac{1}{8\pi(1-\nu)}\oint_C b_i \epsilon_{ijk}\frac{\partial^3 R}{\partial x_l \partial x'_m \partial x'_j}\, dx'_k \tag{A.5}$$

Using Stokes' theorem, the derivative of the solid angle expressed in equation (A.4) can be reduced to the following line integral [18]:

$$\frac{\partial\Omega}{\partial x_l} = \frac{1}{2}\int_S \frac{\partial}{\partial x_l}\frac{\partial^3 R}{\partial x'_p \partial x'_p \partial x'_j}\, dS_j = -\frac{1}{2}\int_C \epsilon_{jlk}\frac{\partial^3 R}{\partial x'_p \partial x'_p \partial x'_j}\, dx'_k \tag{A.6}$$

Denoting $R_{,i} = \partial R/\partial x_i$ and noting that

$$\begin{aligned}\frac{\partial^2 R}{\partial x'_i \partial x'_j} &= \frac{\partial^2 R}{\partial x_i \partial x_j} = R_{,ij} \\ \frac{\partial^3 R}{\partial x'_i \partial x'_j \partial x'_k} &= -\frac{\partial^3 R}{\partial x_i \partial x_j \partial x_k} = -R_{,ijk}\end{aligned} \tag{A.7}$$

expression (A.5) can finally rewrite as

$$\begin{aligned}u_{m,l}(\boldsymbol{x}) = &-\frac{1}{8\pi}\oint_C b_m \epsilon_{jlk} R_{,ppj} dx'_k - \frac{1}{8\pi}\oint_C b_i \epsilon_{mik} R_{,ppl}\, dx'_k \\ &-\frac{1}{8\pi(1-\nu)}\oint_C b_i \epsilon_{ijk} R_{,mjl}\, dx'_k\end{aligned} \tag{A.8}$$

## Appendix B. Analytical non-singular displacement gradient

Following the non-singular theory of dislocations proposed by Cai *et al.* [16], the singularity at the dislocation core can be eliminated by adopting the non-singular radius vector $R_a$ expressed as:

$$R_a = \sqrt{R^2 + a^2} = \sqrt{R_i R_i + a^2} = \sqrt{(x'_i - x_i)(x'_i - x_i) + a^2} \tag{B.1}$$

where parameter $a$ –denoting the core width– is introduced, and where $R = \|\boldsymbol{x'} - \boldsymbol{x}\|$ is the original radius vector. One advantage of choosing the form for $R_a$ given in (B.1) lies in the fact that its derivatives follow the original expressions for that of $R$, i.e. one has:

$$\begin{aligned}R_{a,i} &= -\frac{R_i}{R_a} \\ R_{a,ij} &= \left(\delta_{ij} - \frac{R_i}{R_a}\frac{R_j}{R_a}\right)/R_a \\ R_{a,ijk} &= \left[-3\frac{R_i}{R_a}\frac{R_j}{R_a}\frac{R_k}{R_a} + \left(\delta_{ij}\frac{R_k}{R_a} + \delta_{jk}\frac{R_i}{R_a} + \delta_{ki}\frac{R_j}{R_a}\right)\right]/R_a^2\end{aligned} \tag{B.2}$$

When dislocation loop $C$ with Burgers vector $\boldsymbol{b}$ is approximated by a polygonal loop composed of straight dislocation segments, the displacement gradient in expression (B.3) can be written for each segment defined between end points $\boldsymbol{x}_1$ and $\boldsymbol{x}_2$ as:

$$u_{m,l}(\boldsymbol{x}) = -\frac{1}{8\pi} b_m \epsilon_{jlk} A_{jk}(\boldsymbol{x}) - \frac{1}{8\pi} b_i \epsilon_{mik} A_{lk}(\boldsymbol{x}) - \frac{1}{8\pi(1-\nu)} b_i \epsilon_{ijk} B_{jklm}(\boldsymbol{x}) \tag{B.3}$$

where

$$A_{jk}(\boldsymbol{x}) = \int_{\boldsymbol{x}_1}^{\boldsymbol{x}_2} R_{a,ppj}\, dx'_k \tag{B.4}$$

$$B_{jklm}(\boldsymbol{x}) = \int_{\boldsymbol{x}_1}^{\boldsymbol{x}_2} R_{a,mjl}\, dx'_k \tag{B.5}$$

A coordinate-independent analytical expression of (B.3) can be obtained as follows. As depicted in figure B.8, if one denotes $\boldsymbol{x}_0$ the orthogonal projection of field point $\boldsymbol{x}$ on the dislocation line, the following segment parametric representation can be used:

$$\boldsymbol{d} = \boldsymbol{x}_0 - \boldsymbol{x} \quad \text{with} \quad \boldsymbol{d} \cdot \boldsymbol{t} = 0 \tag{B.6}$$

$$\text{such that} \quad \boldsymbol{d} = \boldsymbol{R} - (\boldsymbol{R} \cdot \boldsymbol{t})\boldsymbol{t} \tag{B.7}$$

where $\boldsymbol{d}$ is the constant vector linking the field point $\boldsymbol{x}$ to its projection $\boldsymbol{x}_0$, such that $d = \|\boldsymbol{d}\|$ is the distance from the field point to the segment, and $\boldsymbol{t}$ is the unit tangent vector to the segment defined by:

$$\boldsymbol{t} = \frac{\boldsymbol{x_2} - \boldsymbol{x_1}}{\|\boldsymbol{x_2} - \boldsymbol{x_1}\|} \tag{B.8}$$

With this, the dislocation segment $\boldsymbol{x'}$ can be conveniently described with the following parametric representation:

$$\boldsymbol{x'} = \boldsymbol{x}_0 + s\boldsymbol{t} \tag{B.9}$$

where the bounds for parameter $s$ are given by:

$$s_1 = (\boldsymbol{x}_1 - \boldsymbol{x}_0) \cdot \boldsymbol{t} \tag{B.10}$$

$$s_2 = (\boldsymbol{x}_2 - \boldsymbol{x}_0) \cdot \boldsymbol{t} \tag{B.11}$$

With this setting, the original radius vector $\boldsymbol{R} = \boldsymbol{x'} - \boldsymbol{x}$ and its non-singular norm $R_a$ can be expressed as:

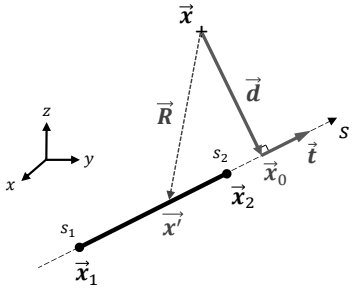


Figure B.8: Parametrization used to describe the straight dislocation segment between end points $\boldsymbol{x}_1$ and $\boldsymbol{x}_2$. Point $\boldsymbol{x}_0$ is the orthogonal projection of field point $\boldsymbol{x}$ on the dislocation line. The unit tangent $\boldsymbol{t}$ and vector $\boldsymbol{d} = \boldsymbol{x}_0 - \boldsymbol{x}$ form an orthogonal basis, such that coordinate $\boldsymbol{x'} = \boldsymbol{x}_0 + s\boldsymbol{t}$ spans segment 12 and the radius vector is defined by $\boldsymbol{R} = \boldsymbol{d} + s\boldsymbol{t}$ with $s \in [s_1, s_2]$.

$$\boldsymbol{R} = \boldsymbol{d} + s\boldsymbol{t} \tag{B.12}$$

$$R_a = \sqrt{\boldsymbol{R} \cdot \boldsymbol{R} + a^2} = \sqrt{\boldsymbol{d} \cdot \boldsymbol{d} + s^2 + a^2} \tag{B.13}$$

such that $R_a$ is solely a function of parameter $s$, both other terms being known constants associated with the segment.

In expression (B.4), the third derivative of the non-singular radius vector is obtained from expression (B.2) as:

$$\begin{aligned} R_{a,ppj} &= -3\frac{R_p R_p R_j}{R_a^5} + \delta_{pp}\frac{R_j}{R_a^3} + \delta_{pj}\frac{R_p}{R_a^3} + \delta_{jp}\frac{R_p}{R_a^3} \\ &= \left(\frac{3a^2}{R_a^5} + \frac{2}{R_a^3}\right) R_j \end{aligned} \tag{B.14}$$

where the identity $R_p R_p = R^2 = R_a^2 - a^2$ is used. Combining the parametric representation introduced in equation (B.9) with expression (B.14), the first integral in (B.4) is expressed as:

$$A_{jk}(\boldsymbol{x}) = t_k \int_{s_1}^{s_2} \left(\frac{3a^2}{R_a^5} + \frac{2}{R_a^3}\right) R_j ds \tag{B.15}$$

where $R_j$ denotes the $j$-th component of the radius vector, such that one has:

$$R_j = \boldsymbol{R} \cdot \boldsymbol{e}_j = d_j + s t_j \tag{B.16}$$

where $d_j$ et $t_j$ denote the $j$-th components of vectors $\boldsymbol{d}$ and $\boldsymbol{t}$, respectively. Consequently, integral (B.15) can be written as:

$$A_{jk}(\boldsymbol{x}) = t_k \left[3a^2 d_j J_{05} + 2d_j J_{03} + 3a^2 t_j J_{15} + 2t_j J_{13}\right] \tag{B.17}$$

where $J_{ij}$ denotes the following line integral:

$$J_{ij} = \int_{s_1}^{s_2} \frac{s^i}{R_a^j} ds \tag{B.18}$$

Similarly, the second integral in (B.5) can be written as:

$$\begin{aligned} B_{jklm}(\boldsymbol{x}) &= t_k \int_{s_1}^{s_2} \left( -\frac{3R_m R_j R_l}{R_a^5} + \delta_{mj}\frac{R_l}{R_a^3} + \delta_{jl}\frac{R_m}{R_a^3} + \delta_{lm}\frac{R_j}{R_a^3} \right) ds \\ &= t_k \left[ (\delta_{mj} d_l + \delta_{jl} d_m + \delta_{lm} d_j) J_{03} + (\delta_{mj} t_l + \delta_{jl} t_m + \delta_{lm} t_j) J_{13} \right. \\ &\quad -3(d_m d_j d_l) J_{05} - 3(d_m d_j t_l + d_m t_j d_l + t_m d_j d_l) J_{15} \\ &\quad \left. -3(d_m t_j t_l + t_m d_j t_l + t_m t_j d_l) J_{25} - 3(t_m t_j t_l) J_{35} \right] \end{aligned} \tag{B.19}$$

With expressions (B.17) and (B.19), the deformation gradient in (B.3) produced by a dislocation segment only depends on specific line integrals $J_{ij}$ that can be evaluated analytically as follows:

$$\begin{aligned} J_{03} &= \int_{s_1}^{s_2} \frac{1}{R_a^3} ds = \left. \frac{s}{(\boldsymbol{d}\cdot\boldsymbol{d} + a^2) R_a} \right|_{s_1}^{s_2} \\ J_{13} &= \int_{s_1}^{s_2} \frac{s}{R_a^3} ds = \left. -\frac{1}{R_a} \right|_{s_1}^{s_2} \\ J_{05} &= \int_{s_1}^{s_2} \frac{1}{R_a^5} ds = \left. \frac{2s^3}{3(\boldsymbol{d}\cdot\boldsymbol{d} + a^2)^2 R_a^3} \right|_{s_1}^{s_2} + \left. \frac{s}{(\boldsymbol{d}\cdot\boldsymbol{d} + a^2) R_a^3} \right|_{s_1}^{s_2} \\ J_{15} &= \int_{s_1}^{s_2} \frac{s}{R_a^5} ds = \left. -\frac{1}{3R_a^3} \right|_{s_1}^{s_2} \\ J_{25} &= \int_{s_1}^{s_2} \frac{s^2}{R_a^5} ds = \left. \frac{s^3}{3(\boldsymbol{d}\cdot\boldsymbol{d} + a^2) R_a^3} \right|_{s_1}^{s_2} \\ J_{35} &= \int_{s_1}^{s_2} \frac{s^3}{R_a^5} ds = \left. -\frac{2(\boldsymbol{d}\cdot\boldsymbol{d} + a^2)}{3R_a^3} \right|_{s_1}^{s_2} - \left. \frac{s^2}{R_a^3} \right|_{s_1}^{s_2} \end{aligned} \tag{B.20}$$

## Appendix C. Conditional convergence of the displacement gradient field in periodic cells

This appendix deals with the issue of conditional convergence that arises when evaluating the displacement gradient field $u_{i,j}$ in a periodic simulation volume. Let us consider an arbitrary dislocation structure composed of $N_{\text{seg}}$ dislocation segments contained in a primary simulation volume (supercell) of length

$L_x, L_y, L_z$ with periodic vectors $\boldsymbol{c}_1, \boldsymbol{c}_2, \boldsymbol{c}_3$. Using equation (14), the total displacement gradient at field point $\boldsymbol{x}$ is obtained by calculating:

$$u_{i,j}^{\mathrm{tot}}(\boldsymbol{x}) = \sum_{\boldsymbol{R}} \sum_{\alpha\beta}^{N_{\mathrm{seg}}} u_{i,j}^{\alpha\beta}(\boldsymbol{x} - \boldsymbol{R}) \tag{C.1}$$

where the inner sum is carried over all dislocation segments $\alpha\beta$ contained within the primary supercell, and the outer sum runs over periodic lattice vectors $\boldsymbol{R} = n_1\boldsymbol{c}_1 + n_2\boldsymbol{c}_2 + n_3\boldsymbol{c}_3$ ($n_i$ are integers) specifying the position of the image dislocation segments with respect to their primary counterparts.

In practice, the sum in equation (C.1) is truncated to a finite number of periodic images $N_{\mathrm{img}}$ in each direction (e.g. $n_i \in \{-(N_{\mathrm{img}}-1)/2, ..., (N_{\mathrm{img}}-1)/2\}$ with $|n_i| = N_{\mathrm{img}},\ \forall i \in \{1,2,3\}$). As a naive approach, the number of images $N_{\mathrm{img}}$ is typically chosen as a tradeoff between the accuracy and the computational cost. However, such a strategy implicitly relies on the assumption that increasing the number of images will tend to improve the accuracy of the calculation. Mathematically however, this is not guaranteed, as the periodic sum of the deformation gradient produced by a collection of finite dislocation segments is not absolutely convergent [19].

This can be seen by examining the expression for the deformation gradient provided in equation (13). The deformation gradient $u_{i,j}$ for an elementary segment behaves as $R^{-2}$ at large $R$. Consequently, the lattice sum of the absolute values of $u_{i,j}(\boldsymbol{x})$ produced at any field point $\boldsymbol{x}$ by an elementary dislocation segment diverges:

$$|u_{i,j}^{\mathrm{sum}}(\boldsymbol{x})| = \sum_{\boldsymbol{R}} |u_{i,j}(\boldsymbol{x} - \boldsymbol{R})| \propto \int^{\infty} dR\, 4\pi R^2 \frac{1}{R^2} \propto \int^{\infty} dR \sim \infty \tag{C.2}$$

and expression (C.1) cannot be readily employed, but needs to be regularized. Following the regularization approach proposed in [19], one can observe that the second derivatives of the deformation gradient $\partial_k \partial_l u_{i,j}$ are proportional to $1/R^4$, and their sum converges absolutely. This implies that the conditional convergence can produce, at worst, a spurious linear term that depends on the order and truncation of the summation. In other words, it means that the lattice sum of the deformation gradient can be written as:

$$u_{i,j}^{\mathrm{tot}}(\boldsymbol{x}) = u_{i,j}^{\mathrm{PBC}}(\boldsymbol{x}) + D_{ijk}x_k + u_{i,j}^{0} \tag{C.3}$$

where $u_{i,j}^{\mathrm{PBC}}(\boldsymbol{x})$ is the correct periodic displacement gradient field, $D_{ijk}$ is a constant third order tensor quantifying the linear error term, and $u_{i,j}^{0}$ is the volume average of displacement gradient over the primary cell. The regularized convergent solution $u_{i,j}^{\mathrm{PBC}}(\boldsymbol{x})$ is then simply obtained by evaluating the $D_{ijk}$ and $u_{i,j}^{0}$

tensors. $D_{ijk}$ is measured by evaluating the displacement gradient at the edges of the simulation supercell, e.g.:

$$\begin{aligned} D_{ij1} &= \left[ u_{i,j}\left(\frac{L_x}{2},0,0\right) - u_{i,j}\left(-\frac{L_x}{2},0,0\right)\right]/L_x \\ D_{ij2} &= \left[ u_{i,j}\left(0,\frac{L_y}{2},0\right) - u_{i,j}\left(0,-\frac{L_y}{2},0\right)\right]/L_y \\ D_{ij3} &= \left[ u_{i,j}\left(0,0,\frac{L_z}{2}\right) - u_{i,j}\left(0,0,-\frac{L_z}{2}\right)\right]/L_z \end{aligned} \tag{C.4}$$

while $u^0_{i,j}$ is directly obtained by averaging the value of the displacement gradient over all sampling points. With this, the regularized solution is finally obtained at every field point $\boldsymbol{x}$ as:

$$u^{\mathrm{PBC}}_{i,j}(\boldsymbol{x}) = u^{\mathrm{tot}}_{i,j}(\boldsymbol{x}) - D_{ijk}x_k - u^0_{i,j} \tag{C.5}$$

which is guaranteed to be periodic and to have zero volume average.

## References


[1] G. E. Ice, B. C. Larson, 3D X-Ray crystal microscope, Advanced Engineering Materials 2 (10) (2000) 643–646.

[2] B. Larson, W. Yang, G. Ice, J. Budai, J. Tischler, Three-dimensional X-ray structural microscopy with submicrometre resolution, Nature 415 (6874) (2002) 887–890.

[3] N. Tamura, R. Celestre, A. MacDowell, H. Padmore, R. Spolenak, B. Valek, N. Meier Chang, A. Manceau, J. Patel, Submicron x-ray diffraction and its applications to problems in materials and environmental science, Review of scientific instruments 73 (3) (2002) 1369–1372.

[4] R. Maaß, S. Van Petegem, H. Van Swygenhoven, P. M. Derlet, C. A. Volkert, D. Grolimund, Time-resolved laue diffraction of deforming micropillars, Physical review letters 99 (14) (2007) 145505.

[5] I. Robinson, R. Harder, Coherent x-ray diffraction imaging of strain at the nanoscale, Nature materials 8 (4) (2009) 291–298.

[6] B. E. Warren, X-Ray Diffraction, Dover, 1969.

[7] B. D. Cullity, S. R. Stock, Elements of X-Ray Diffraction, 3rd Edition, Prentice Hall, 2001.

[8] G. Ice, R. Barabash, Chapter 79 white beam microdiffraction and dislocations gradients, Dislocations in Solids 13 (2007) 499 – 601.

[9] A. Arsenlis, W. Cai, M. Tang, M. Rhee, T. Oppelstrup, G. Hommes, T. G. Pierce, V. V. Bulatov, Enabling strain hardening simulations with dislocation dynamics, Modelling and Simulation in Materials Science and Engineering 15 (6) (2007) 553–595.

[10] R. B. Sills, A. Aghaei, W. Cai, Advanced time integration algorithms for dislocation dynamics simulations of work hardening, Modelling and Simulation in Materials Science and Engineering 24 (4) (2016) 045019.

[11] Z. Wang, R. J. McCabe, N. M. Ghoniem, R. LeSar, A. Misra, T. E. Mitchell, Dislocation motion in thin cu foils: a comparison between computer simulations and experiment, Acta Materialia 52 (6) (2004) 1535 – 1542.

[12] F. Hofmann, S. Eve, J. Belnoue, J.-S. Micha, A. M. Korsunsky, Analysis of strain error sources in micro-beam laue diffraction, Nuclear Instruments and Methods in Physics Research Section A: Accelerators, Spectrometers, Detectors and Associated Equipment 660 (1) (2011) 130 – 137.

[13] F. Hofmann, S. Keegan, A. M. Korsunsky, Diffraction post-processing of 3d dislocation dynamics simulations for direct comparison with micro-beam laue experiments, Materials Letters 89 (2012) 66 – 69.

[14] L. Balogh, L. Capolungo, C. Tome, On the measure of dislocation densities from diffraction line profiles: A comparison with discrete dislocation methods, Acta Materialia 60 (4) (2012) 1467 – 1477.

[15] M. V. Upadhyay, L. Capolungo, L. Balogh, On the computation of diffraction peaks from discrete defects in continuous media: comparison of displacement and strain-based methods, Journal of Applied Crystallography 47 (3) (2014) 861–878.

[16] W. Cai, A. Arsenlis, C. R. Weinberger, V. V. Bulatov, A non-singular continuum theory of dislocations, Journal of the Mechanics and Physics of Solids 54 (3) (2006) 561–587.

[17] J.-S. Chung, G. E. Ice, Automated indexing for texture and strain measurement with broad-bandpass x-ray microbeams, Journal of Applied Physics 86 (9) (1999) 5249–5255.

[18] J. Hirth, J. Lothe, Theory of Dislocations, Krieger Publishing Company, Malabar, Florida, 1982.

[19] W. Cai, V. V. Bulatov, J. Chang, J. Li, S. Yip, Periodic image effects in dislocation modelling, Philosophical Magazine 83 (5) (2003) 539–567.

[20] W. T. Read, W. Shockley, Dislocation models of crystal grain boundaries, Phys. Rev. 78 (1950) 275–289.